



High Lithium Abundance Connection with the Chromospheric Helium in Red Giants: Spectroscopic and Asteroseismic Analyses

Anohita Mallick^{1,2} , Christopher Sneden³ , Bacham E. Reddy^{1,4} , and Melike Afşar⁵ ¹ Indian Institute of Astrophysics, 560034, 100ft road Koramangala, Bangalore, India; anohitamallick@gmail.com, bachamr@gmail.com² Pondicherry University, R. V. Nagara, Kala Pet, 605014, Puducherry, India³ Department of Astronomy and McDonald Observatory, The University of Texas, Austin, TX 78712, USA⁴ Department of Physics, Indian Institute of Technology Jammu, Jammu 181221, India⁵ Department of Astronomy and Space Sciences, Ege University, 35100 Bornova, İzmir, Türkiye

Received 2024 December 5; revised 2025 January 13; accepted 2025 January 14; published 2025 February 20

Abstract

We present a study of correlations between high Li abundances and strong chromospheric He I $\lambda 10830$ absorption-line strengths in Kepler field giant stars. Our sample includes 84 giants with detectable solar-like oscillations in their light curves, and their Li abundances come from the literature or are measured here using LAMOST medium-resolution spectra. Evolutionary phases are determined through asteroseismic analysis, with mixed-mode period spacing (ΔP) used to infer the time evolution of red clump (RC) giants. Near-IR observations of the He I $\lambda 10830$ line were obtained with the high-resolution Habitable-zone Planet Finder spectrograph on the Hobby–Eberly Telescope. We find high Li abundances and strong He I lines exclusively among RC giants, with their absence in red giant branch stars suggesting a shared origin linked to the He flash. Additionally, a steady decline in He I strength with decreasing Li abundance among RC giants indicates a correlation between these properties. Older, Li-normal RC giants are He weak, while most younger, super-Li-rich giants are He strong, suggesting temporal evolution of both phenomena. We hypothesize that the core He flash and subsequent subflashes may enhance Li abundances in RC giant photospheres and trigger heightened chromospheric activity, leading to stronger He I $\lambda 10830$ lines in younger RCs. Over time, following He flash, chromospheric activity diminishes, resulting in weaker He I lines in older, Li-normal RCs.

Unified Astronomy Thesaurus concepts: Red giant clump (1370); Stellar oscillations (1617); Stellar abundances (1577); Stellar chromospheres (230); Helium burning (716)

Materials only available in the [online version of record](#): machine-readable table

1. Introduction

Lithium (Li) is one of the elements known to have primordial origin. Standard big bang nucleosynthesis (BBN) theories predict $A(\text{Li}) \simeq 2.72$ dex,⁶ generally considered to be the primordial value (R. H. Cyburt et al. 2008). The measured high values of Li abundance of $A(\text{Li}) > 3.2$ dex in very young stars or in the interstellar medium suggest that the Galaxy has been enriched with additional Li since the big bang (M. Asplund et al. 2009). Cosmic-ray spallation (CRS) and stellar nucleosynthesis are two of the major sources identified for Li enrichment in the Galaxy. CRS alone seems to be inadequate to explain the fourfold increase in Li (H. E. Mitler 1972; D. Romano et al. 2001). Moreover, canonical models do not predict Li production in stars (I. J. Iben 1968). In general, stars are considered as Li sinks, and the observations largely comply with the theory (M. H. Pinsonneault et al. 2000). Spectroscopic studies conducted over the past five decades have identified a small subset of evolved stars with exceptionally high Li abundances. These include intermediate-mass asymptotic giant branch (AGB) (V. V. Smith et al. 1995; N. Holanda et al. 2020)

and low-mass red giant branch (RGB) stars (Y. B. Kumar et al. 2011; J. M. Alcalá et al. 2011; S. L. Martell et al. 2021). The high Li in AGB stars is attributed to hot bottom burning (I. J. Sackmann & A. I. Boothroyd 1992). In contrast, the origin of high Li in low-mass red giants remains an unresolved puzzle since its discovery (G. Wallerstein & C. Sneden 1982).

Significant progress has been made in this area recently, driven by large-scale spectroscopic surveys. Studies have identified many Li-rich giants (LRGs) with Li abundances more than $A(\text{Li}) \simeq 1.5$ dex, an upper limit set by standard theories for giants. There are now a few hundred LRGs, and among those a few dozen are super-Li-rich (SLR) giants with abundance $A(\text{Li}) \geq 3.2$ dex (Y. B. Kumar et al. 2011; Deepak & B. E. Reddy 2019; R. Singh et al. 2019; L. Magrini et al. 2021; H.-L. Yan et al. 2021). Following the suggestion of Y. B. Kumar et al. (2011) that Li production may be linked to the He flash at the tip of the RGB, studies focusing on identifying the evolutionary phase of LRGs revealed that the majority of LRGs are red clump (RC) giants (A. R. Casey et al. 2019; Y. B. Kumar et al. 2020). Interestingly, all the SLR giants for which evolutionary phases have been determined using asteroseismic analysis are found to be in the He core burning phase (R. Singh et al. 2019, 2021). Studies show strong circumstantial evidence that the high Li abundance among RC giants may have originated during the short phase of He flash (Y. B. Kumar et al. 2020; S. L. Martell et al. 2021; R. Singh et al. 2021; C. Sneden et al. 2022; A. Mallick et al. 2023).

⁶ For elements X and Y, $A(X) \equiv \log \epsilon(X) = \log (N_X/N_H) + 12.0$, and $[X/Y] = \log (N_X/N_Y)_* - \log (N_X/N_Y)_\odot$. Metallicity will normally be assumed to be the $[\text{Fe}/\text{H}]$ value.



The physical mechanism of Li production and mixing processes during the He flash phase are not well understood. In addition, it is not clear whether the He flash is the sole source of high Li among RC giants. There are few observations showing very high Li abundance among giants on the RGB, particularly among clusters (G. R. Ruchti et al. 2011; E. N. Kirby et al. 2016; L. Magrini et al. 2021; M. Tsantaki et al. 2023). If this is true, one needs to understand whether there are multiple sites for Li production in red giants. It would be worth determining the evolutionary phase of some of these RGB LRGs using asteroseismic data.

Here we investigate whether the LRGs have any other unique observational characteristics. One possibility is He line strength, a concept first suggested by the serendipitous discovery of a strong chromospheric He I $\lambda 10830$ absorption feature in a Li-rich ($A(\text{Li}) > 1.5$ dex) red giant (see C. Sneden et al. 2021). A subsequent survey by C. Sneden et al. (2022) found that $\sim 56\%$ of Li-rich field giants in their sample have similarly strong He I $\lambda 10830$ absorption features. This has opened a new avenue for uncovering further clues about the high Li abundances observed in a small fraction of red giants. In this paper we explore a further possible link: red giant evolutionary state from asteroseismological signatures. We present Li abundances, He I $\lambda 10830$ line strengths, and asteroseismic parameters for 84 Kepler field giants. In Section 2, we discuss the stellar sample selection criteria. Section 3 describes Li abundance measurements obtained from LAMOST spectra, and Section 4 covers the acquisition and reduction of high-resolution He I $\lambda 10830$ spectra. In Section 5, we investigate the asteroseismic properties of the selected red giants, while Section 6 examines the variations in helium and Li among different evolutionary stages. Finally, Section 7 explores potential infrared excess, binarity, and other chromospheric activity indicators.

2. Sample Selection

Our observational task was to gather high-resolution spectra of He I $\lambda 10830$ transitions in red giants that have asteroseismic data and either measured Li abundances or spectra from which they can be derived. Following groundbreaking space-based asteroseismology efforts of the MOST (G. Walker et al. 2003) and CoRoT (C. Catala & CoRoT Team 2001) projects, the NASA Kepler mission (W. J. Borucki et al. 2010) observed more than half a million stars, mostly centered on a single 115° field in Cygnus. In its final data release (DR25; J. Coughlin et al. 2017), Kepler detected solar-like oscillations in nearly 22,000 red giant stars (M. Hon et al. 2019). We searched for Kepler giants with published Li abundances, finding many in several recent studies (R. Singh et al. 2019, 2021; H.-L. Yan et al. 2021; Y. Takeda & A. Tajitsu 2017). The Li abundances reported in this work are derived from the LAMOST survey (S.-G. Wang et al. 1996). The methodology employed for this analysis is outlined in Section 3. From this list of Kepler field red giants, we collected near-IR ($z\text{y}J$ band, $8400\text{--}12500$ Å) high-resolution spectra with the Habitable Zone Planet Finder Spectrograph (HPF) on the Hobby-Eberly Telescope (HET). The H-R diagram of the sample, shown in Figure 1, highlights the distribution of these stars across the Kepler field of view.

These spectra were employed to study their He I $\lambda 10830$ lines. We culled the sample to a brightness range of $3 < J_{\text{mag}} < 13$ so that we obtain IR spectra of optimal signal-to-noise ratio (SNR). In the end, we collected HPF spectra for 84 stars (39

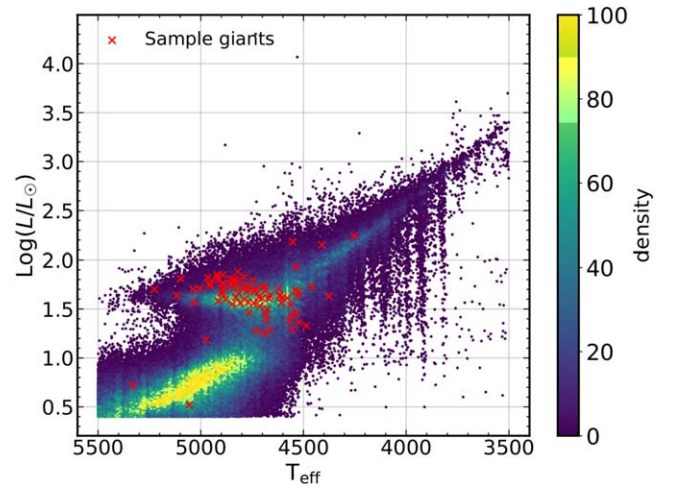


Figure 1. H-R diagram displaying the sample of 84 red giants (red crosses). The entire sample from the Kepler Input Catalog (KIC) is shown in the background. The color bar represents the normalized star density in each region of the plot, with the maximum value scaled to 100. T_{eff} was taken from the KIC (T. M. Brown et al. 2011), and luminosities were calculated using Gaia G -band magnitudes (see R. Andrae et al. 2018).

from the LAMOST survey). The complete sample for our study is provided in Table 1.

3. Lithium Measurements from LAMOST

We have extracted medium-resolution spectra (MRS, $R \approx 7500$) for 39 red giants from the LAMOST survey. Each MRS target provides a pair of spectra within a single exposure, consisting of blue (B) and red (R) band spectra spanning wavelength ranges of $[4950 \text{ \AA}, 5350 \text{ \AA}]$ and $[6300 \text{ \AA}, 6800 \text{ \AA}]$, respectively. We used the R -band spectra as they cover the Li I resonance line at 6707.8 \AA . Coadded spectra are available for all objects. All spectra have SNRs in the R band exceeding 35, which is sufficient for abundance calculations.

The spectral data were brought to rest wavelength by correcting for stars' radial velocity (RV) and continuum normalized using standard IRAF procedures. RVs are taken from Gaia DR3 (D. Katz et al. 2023). The stellar parameters T_{eff} , $\log g$, and $[\text{Fe}/\text{H}]$ are extracted from the LAMOST MRS parameter catalog estimated by the LAMOST stellar parameter pipeline (LASP; M. S. Xiang et al. 2015). The microturbulent velocities (ξ) are estimated from empirical relations provided by J. A. Holtzman et al. (2018) and A. E. García Pérez et al. (2016). Utilizing these parameters, stellar atmospheric models were generated using the ATLAS9 code developed by F. Castelli & R. L. Kurucz (2003). Synthetic spectra were generated for each star based on their respective stellar parameters using the Python wrapper of the LTE radiative transfer code MOOG (C. A. Sneden 1973), `pyMOOGi`.⁷ Li abundances were adjusted in each spectrum to achieve the best fit with the observed spectra, minimizing the χ^2 statistic. The resulting Li abundance $A(\text{Li})$ was adopted as the final value for the program star. Figure 2 illustrates the spectra of selected giants analyzed in this study. Panel (a) shows representative spectra from LAMOST, highlighting the Li resonance line at 6707.8 \AA and the strong Ca line at 6717.7 \AA . Panel (b) contrasts spectrum synthesis for the stars with the lowest and highest Li abundances in our sample, demonstrating the spectral features

⁷ <https://github.com/madamow/pymoogi>

Table 1
Derived and Adopted Parameters of the Kepler Sample

KIC	T_{eff} (K)	$\log g$ (dex)	[Fe/H] (dex)	$A(\text{Li})$ (dex)	Source	EW_{He} (mÅ)	RW_{He} (dex)	RUWE (dex)	ν_{max} (μHz)	$\Delta\nu$ (μHz)	ΔP (s)	Evol Stage ^a	Mass (M_{\odot})	$\log\left(\frac{L}{L_{\odot}}\right)$ (L_{\odot})	$(B - V)$ (dex)	$\log R'_{\text{HK}}$ (dex)
1726211	4965 ± 95	2.24 ± 0.06	-0.61 ± 0.03	-0.03 ± 0.17	3	105 ± 15	-5.01 ± 0.06	0.90	30.40 ± 0.63	3.72 ± 0.05	321.66 ± 6.50	1	1.44 ± 0.35	1.82	0.98 ± 0.19	-5.43 ± 0.50
2305930	4879 ± 25	2.47 ± 0.06	-0.39 ± 0.03	3.90 ± 0.03	4	300 ± 10	-4.56 ± 0.01	0.91	27.92 ± 0.94	3.77 ± 0.10	297.12 ± 10.00	1	0.74 ± 0.13	1.60	1.18 ± 0.20	-5.36 ± 0.29
2449858	4840 ± 30	2.50 ± 0.10	-0.15 ± 0.00	3.30 ± 0.28	1	195 ± 10	-4.74 ± 0.02	0.95	26.76 ± 0.45	3.46 ± 0.05	215.00 ± 6.60	1	1.23 ± 0.12	1.80	1.18 ± 0.02	-5.37 ± 0.03
2714397	5003 ± 100	2.44 ± 0.01	-0.62 ± 0.15	0.00 ± 0.19	3	50 ± 10	-5.34 ± 0.09	1.02	33.08 ± 0.52	4.18 ± 0.04	319.22 ± 3.46	1	1.10 ± 0.06	1.71	1.04 ± 0.15	-5.40 ± 0.28
3748691	4954 ± 100	2.50 ± 0.01	0.07 ± 0.15	0.00 ± 0.26	3	69 ± 10	-5.20 ± 0.06	0.84	38.71 ± 0.79	4.24 ± 0.05	321.61 ± 3.97	1	1.63 ± 0.07	1.76	0.81 ± 0.36	-5.40 ± 1.84
3751167	4914 ± 80	2.33 ± 0.03	-0.76 ± 0.15	4.00 ± 0.57	1	330 ± 15	-4.52 ± 0.02	1.02	26.14 ± 1.59	3.59 ± 0.12	268.52 ± 17.60	1	0.95 ± 0.22	1.80	1.23 ± 0.20	-4.82 ± 0.28
3858850	4375 ± 14	2.23 ± 0.03	0.29 ± 0.02	2.95 ± 0.09	4	195 ± 10	-4.74 ± 0.02	0.96	25.92 ± 0.69	3.48 ± 0.07	285.00 ± 15.70	1	0.95 ± 0.11	1.63	1.32 ± 0.14	-5.62 ± 0.25
4044238	4702 ± 164	2.44 ± 0.01	0.00 ± 0.30	1.08 ± 0.35	3	95 ± 8	-5.06 ± 0.04	1.05	34.55 ± 0.75	4.01 ± 0.05	296.40 ± 3.06	1	1.33 ± 0.21	1.61		
4161005	4897 ± 40	2.35 ± 0.10	-0.52 ± 0.00	3.30 ± 0.36	1	415 ± 15	-4.42 ± 0.02	1.02	29.10 ± 0.96	3.90 ± 0.12	257.20 ± 1.89	1	1.03 ± 0.18	1.67	1.09 ± 0.03	-5.38 ± 0.06
4446405	4846 ± 100	2.69 ± 0.01	-0.13 ± 0.15	1.37 ± 0.19	5	165 ± 10	-4.82 ± 0.03	0.89	59.96 ± 0.65	5.75 ± 0.02	81.04 ± 3.90	0	1.58 ± 0.09	1.55	1.33 ± 0.51	-5.66 ± 0.76

Note.

^a 0: RGB; 1: RC; 2: subgiant.

References. (1) R. Singh et al. 2019; (2) R. Singh et al. 2021; (3) Y. Takeda & A. Tajitsu 2017; (4) H.-L. Yan et al. 2021; (5) this work.

(This table is available in its entirety in machine-readable form in the [online article](#).)

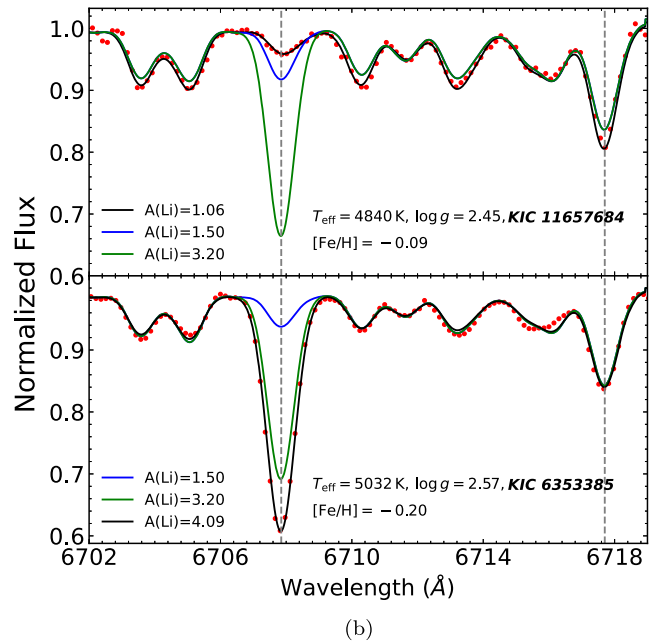
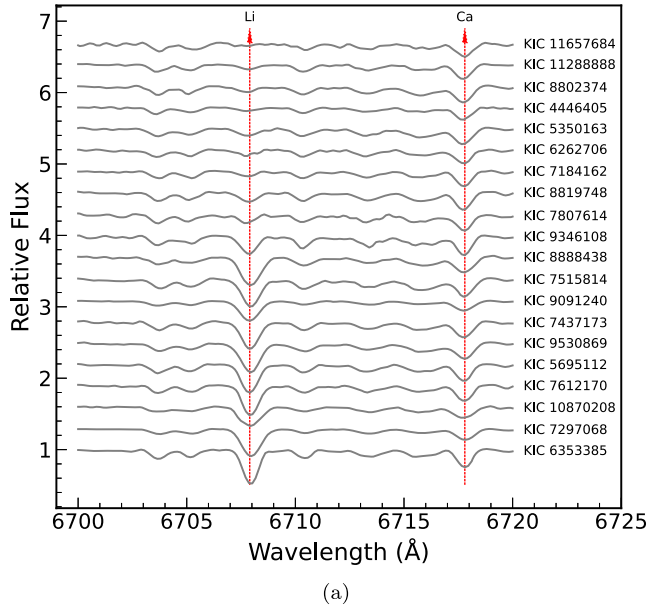


Figure 2. (a) Spectra of a few giants from LAMOST whose Li abundances were measured in this work. (b) Spectrum synthesis for two sample Kepler giants, representing the highest and lowest Li abundances measured. Observed spectra (red circles) are compared with the best-fit models (solid black lines) and additional models to illustrate the significance of Li detection: blue for $A(\text{Li}) = 1.5$ dex (classical Li-rich threshold) and green for $A(\text{Li}) = 3.2$ dex (SLR threshold). The vertical dotted lines indicate the Li resonance line at 6707.8 Å and a strong Ca line at 6717.7 Å.

used to determine $A(\text{Li})$. Derived values of $A(\text{Li})$ for all 39 stars have been provided in Table 1.

4. HPF Observations and Reductions

We gathered high-resolution HET/HPF spectra of 84 Kepler giants. The HPF is a near-IR spectrograph (zyJ photometric bands, 8100–12750 Å). Its development and working parameters have been presented in S. Mahadevan et al. (2012, 2014).⁸ HPF is an echelle spectrograph with 28 fixed spectral orders and resolving power $R \equiv \lambda/\Delta\lambda \sim 55,000$. Our spectra were obtained over a period of about 2 yr. The HPF facility reduction package *Goldilocks*⁹ operated automatically on the raw data frames to produce output files ready for reduction steps. We used IRAF (D. Tody 1986, 1993)¹⁰ routines to accomplish all steps leading to final 2D echelle spectra, including sky emission-line subtraction, order-by-order continuum normalization, telluric absorption-line division, wavelength scale transformation, and correction to rest velocity. In Figure 3 we show example spectra of three of our program stars.

Analysis of the reduced spectra was limited to estimation of rotational velocity and equivalent width (EW) of the $\lambda 10830$ line. To derive these quantities, we followed the methods discussed in detail by C. Sneden et al. (2022; see further discussion by M. Afşar 2025, in preparation). To summarize the procedure briefly, the first step was recognition that the He I $\lambda 10830$ transition arises in red giant chromospheres, not photospheres. This is due to both the 19.8 eV excitation energy of its lower state and the lack of connection to the ground state—it is a metastable level (see, e.g., Figure 3 of G. W. Preston et al. 2022). But as illustrated by the spectrum of KIC 6353385

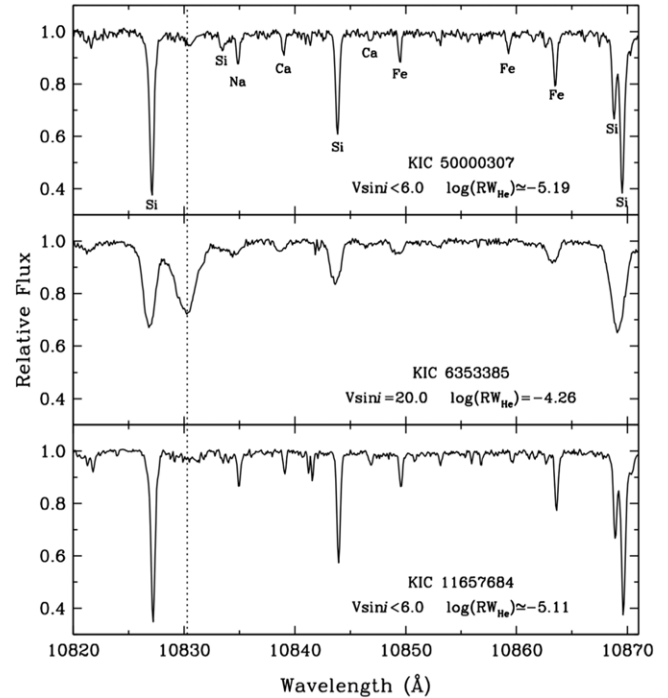


Figure 3. He I $\lambda 10830.3$ spectra of three program stars that appear in other figures of this paper. The HPF spectral order containing the $\lambda 10830$ line extends from about 10820 to 10960 Å, leading to the appearance of $\lambda 10830$ near the blue end of the order. Some prominent atomic features, all due to neutral species transitions, are labeled by element name, while the He I feature is indicated by a dotted vertical line.

in Figure 3, strong $\lambda 10830$ chromospheric lines have significant spectral overlap with nearby photospheric lines, especially Si I $\lambda 10827.1$. The procedure involved creating synthetic spectra to model and remove contaminating photospheric lines near the He I $\lambda 10830$ feature. The EW was then

⁸ See <https://hpf.psu.edu/> for HPF parameter description.

⁹ https://github.com/grzeimann/Goldilocks_Documentation

¹⁰ <https://iraf-community.github.io/>

determined by comparing the observed spectra with the synthetic ones, accounting for various broadening effects, including rotational, instrumental, and macroturbulent. For stars with detectable rotation, additional rotational smoothing was applied to the synthetic spectra, and the broadening parameters were adjusted iteratively to achieve the best match.

5. Asteroseismic Investigation of Kepler Red Giants

5.1. Stellar Pulsation Theory

Solar-like oscillations occur in cool stars with outer convective envelopes. Turbulent motions in their convective zones trigger envelope pulsations deforming the surface. At the end of the RGB phase, stars with masses $\gtrsim 0.8 M_{\odot}$ undergo the He flash, leading to a rapid contraction in size and a decrease in luminosity. Following He flash, stars settle into the core helium burning phase known as the RC (I. J. Iben 1968) or red horizontal branch. These stars occupy a very narrow luminosity range and exhibit slight variations in temperature due to differences in stellar mass and composition. The RC stars in a $T_{\text{eff}} - L$ plot overlap with the giants ascending the RGB (see Figure 1), making it challenging to distinguish between them, especially in field stars. Asteroseismic analysis (T. R. Bedding et al. 2011) has made it possible to accurately distinguish between RGB stars and RC giants. Two key asteroseismic parameters—the p -mode large frequency separation ($\Delta\nu$) and the average period spacing (ΔP) of dipole mixed oscillation modes—can be used to differentiate these two stellar populations. The RC giants generally show higher ΔP than RGBs.

5.2. Data Preparation

Kepler space telescope observations consist of a range of pulsating stars with photometric variations monitored at two cadences: the short cadence of 58.9 s observations, or the long cadence of ~ 29.4 minutes. Evolved RGB stars exhibit $\nu_{\text{max}} \sim 20 \mu\text{Hz}$ (the frequency at which oscillation modes reach maximum power), equivalent to half-day periods, making the 30-minute sampling rate sufficient. In this work, we have used long-cadence light curves, as the long-duration data are useful for detecting low-frequency oscillations and have better mode resolution. For all stars, Kepler provides two types of fluxes: the raw pixel data, which are calibrated and photometrically analyzed (the simple aperture photometry flux with instrumental jitters), and the flux that has been systematically corrected for instrumental perturbations (the pre-search data conditioning simple aperture photometry (PDCSAP) flux; J. C. Smith et al. 2012). Three of our stars do not have Kepler time series data, for which we obtained ~ 30 -minute-cadence data from TESS. Kepler and TESS light curves were processed using the Lightkurve Collaboration et al. (2018)¹¹ package.

Although a quality masking process filters out most bad data points in the time series within the PDCSAP flux, certain issues can persistently affect the light curves. These include fluctuations in flux caused by cosmic rays, zero-crossing events, Argabrightening from detector saturation (J. E. Van Cleve & D. A. Caldwell 2009), deviations due to the loss of fine pointing, and anomalies attributed to rolling band artifacts from detector electronics. A stringent 4.5σ clipping technique was applied to remove outlier data points caused by momentum desaturation (R. Handberg & M. N. Lund 2014). Subsequently, only data

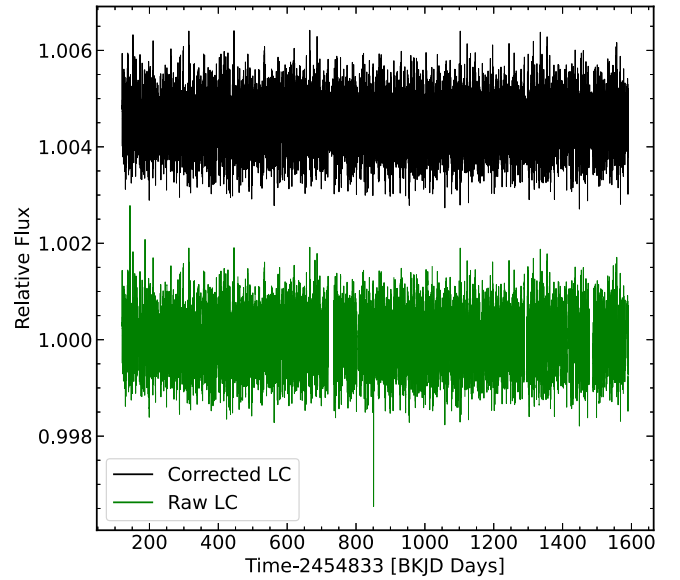


Figure 4. The raw (green) and corrected (black) stitched light curves from Kepler Q0–Q17 quarters for KIC 5000307. The corrected light curve has been vertically offset by 4.5×10^{-2} for comparison.

points with quality flags set to zero were retained. Random white Gaussian noise was introduced to address any resulting data gaps. All the corrected light curves from different quarters were normalized and finally stitched together, which are suitable for asteroseismic analysis. We present raw and corrected stitched light curves for KIC 5000307 in Figure 4 to illustrate the data preparation process critical for asteroseismic analysis.

5.3. Detection of Seismic Parameters

In asteroseismology, time-series data are analyzed in the frequency domain by calculating the power spectral density (PSD). To account for irregularly sampled light curves, the Lomb–Scargle periodogram technique is employed to estimate the PSD (N. R. Lomb 1976; J. D. Scargle 1982). The PSD shows the signal amplitude over a range of frequencies. To estimate ν_{max} , a small region in the background-noise-corrected PSD showing strong power excess is selected. The central peak frequency of this distribution is denoted as ν_{max} . An empirical relation proposed by D. Stello et al. (2009) provides a rough approximation for $\Delta\nu$:

$$\Delta\nu_{\text{est}} = (0.263 \pm 0.009) \nu_{\text{max}}^{(0.772 \pm 0.005)} \mu\text{Hz}.$$

A 2D autocorrelation function (ACF) is computed within the same region that cross-correlates the data with a temporally shifted version of itself. As shown in Figure 5(a), the smoothed 2D ACF derived from the PSD was instrumental in identifying ν_{max} for the example star KIC 5000307. Figure 5(b) shows the ACF peaks near the empirical $\Delta\nu$ estimates for the same.

When analyzing giant stars with low ν_{max} values, a frequency window width narrower than ν_{max} should be chosen to prevent oversmoothing of the PSD. However, Lightkurve cannot accurately fit Gaussians in narrow ranges, which in turn affects the computation of ACF for stars with low ν_{max} . Additionally, it does not support estimating the uncertainties of $\nu_{\text{max}}/\Delta\nu$. To address these challenges, as well as for a recheck on our parameter estimates, we reanalyzed our entire sample with pySYD,¹² an

¹¹ <https://lightkurve.github.io/lightkurve/index.html>

¹² <https://github.com/ashleychontos/pySYD>

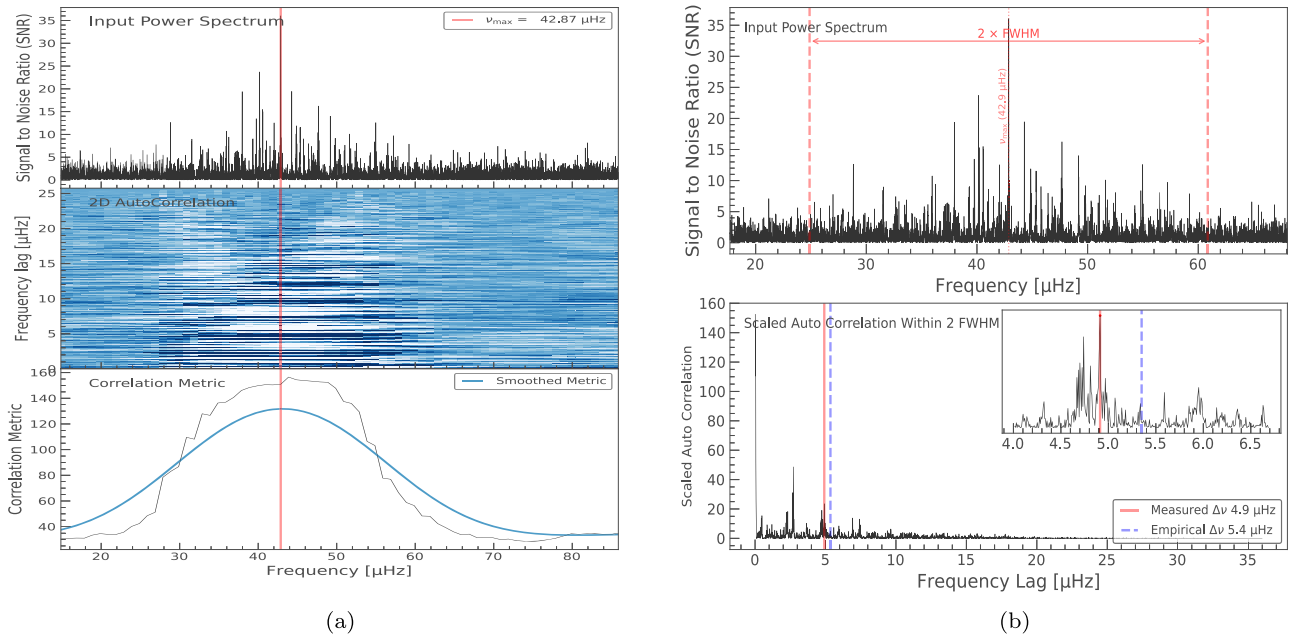


Figure 5. Results of Lightkurve analysis for KIC 5000307. (a) Estimation of ν_{\max} using a smoothed 2D ACF over background-corrected PSD. (b) Peaks in ACF in the region near empirical $\Delta\nu$ for calculating $\Delta\nu$.

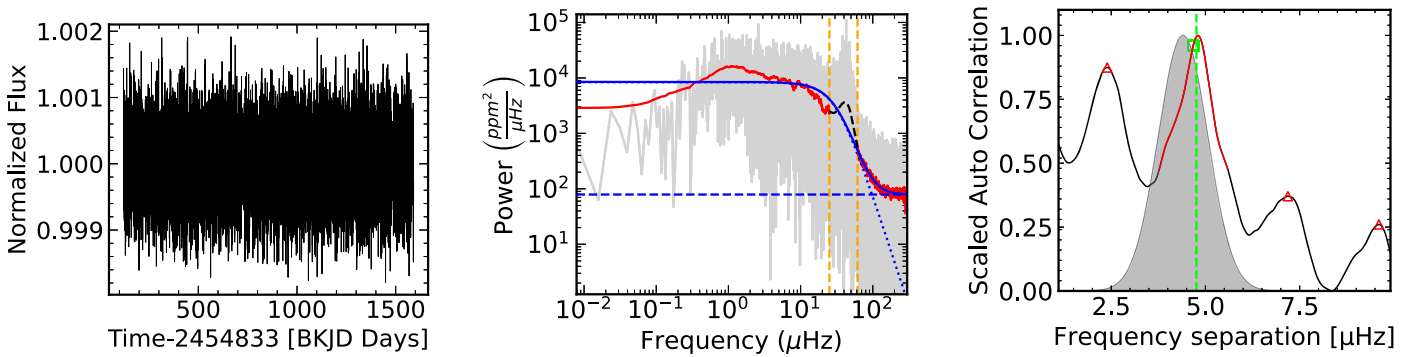


Figure 6. pySYD results for KIC 5000307. The left panel shows the corrected light curve. The middle panel shows the PSD, where the original PSD is shown in gray, the red curve is the smoothed PSD using a boxcar filter of $5 \mu\text{Hz}$, and the black dashed line indicates the Gaussian power excess superposed on the smoothed PSD. The blue dashed line indicates the white noise, the blue dotted line shows stellar granulation, and the solid blue line is the overall best fit to the background. The right panel shows an ACF of a small window of the background-corrected PSD centered on ν_{\max} . The black solid line is the smoothed background-corrected PSD, and the red region indicates the extracted ACF peak. Gray shading represents the Gaussian weighting function to define the red region, and the center of the Gaussian fit (green dashed line) provides the estimated value of $\Delta\nu$.

open-source Python translation of the widely tested IDL-based SYD pipeline (D. Huber et al. 2009) developed by A. Chontos et al. (2022). The primary difference between pySYD and Lightkurve is the modeling of background noise. pySYD employs Harvey-like functions along with white noise to fit the background due to stellar granulation activity. Power spectra of KIC 5000307 with the best-fit background (solid blue line) are illustrated in the middle panel of Figure 6. The process iteratively models the best background fit that minimizes the Bayesian information criterion. Subsequently, the methods for estimating ν_{\max} and $\Delta\nu$ from the background-corrected PSD remain consistent with Lightkurve. For calculating uncertainties a Monte Carlo sampling introduces stochastic noise to the PSD. The background is iteratively fitted to the perturbed PSD, and global seismic parameters are recomputed ~ 200 times. Figure 6 displays the pySYD analysis results for KIC 5000307, including the corrected light curve, background-corrected PSD, and derived seismic parameters, providing

more robust background corrections and uncertainties compared to the results from Lightkurve shown in Figure 5.

For estimating ΔP , the background-corrected PSD is again smoothed using a Gaussian filter ($\sigma \sim 2$). An initial guess of mixed dipole mode ($l = 1$) frequencies is made by identifying peaks in the smoothed flux data by comparing values to their neighbors. Regions are selected containing at least four to five consecutive $l = 1$ modes manually. The periods between consecutive $l = 1$ frequencies are computed. The average and standard error of these periods are propagated as the average mixed mode period spacing ΔP and its uncertainty as illustrated in Figure 7. Seismic parameters for all stars are shown in Table 1.

5.4. Evolutionary Status

In the ΔP - $\Delta\nu$ diagram (Figure 8), RGB stars occupy the lower ΔP regime. Following the classification criteria by

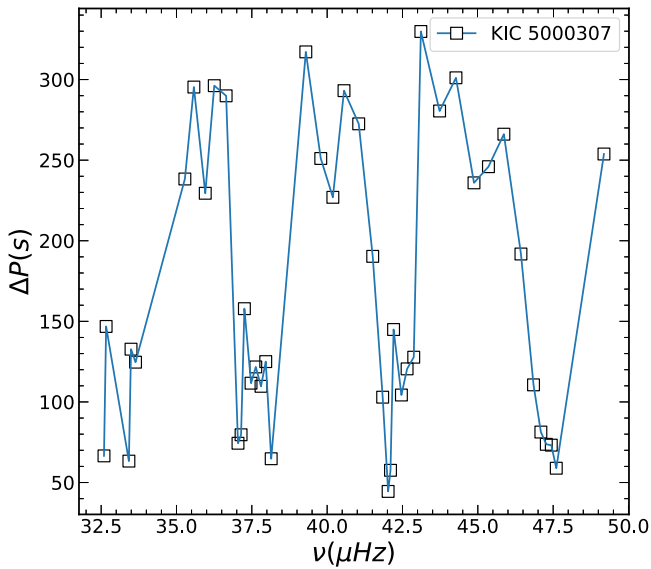


Figure 7. Period spacing for KIC 5000307.

various works (M. Vradar et al. 2016; Y.-S. Ting et al. 2018), we adopted all stars with $\Delta P < 150$ s as red giants in the H-burning phase and stars with $\Delta P \geq 150$ s as RC giants in the core He burning (CHeB) phase. Among the H-burning stars, we have 24 RGB stars and 1 subgiant star (B. Mosser et al. 2014). In total, the sample has 59 CHeB stars, 24 RGB stars, and 1 subgiant star. We calculated seismic stellar masses using the corrected scaling relations given by S. Sharma et al. (2016),

$$\frac{M}{M_{\odot}} \approx \left(\frac{\nu_{\max}}{f_{\nu_{\max}} \nu_{\max, \odot}} \right)^3 \left(\frac{\Delta \nu}{f_{\Delta \nu} \Delta \nu_{\odot}} \right)^{-4} \left(\frac{T_{\text{eff}}}{T_{\text{eff}, \odot}} \right)^{3/2}.$$

6. Helium and Lithium Variations among RGB and CHeB Stars

EWs of the He I $\lambda 10830$ lines for all stars were determined using a spectrum analysis software package SPECTRE¹³ (M. J. Fitzpatrick & C. Sneden 1987). Since there is a significant variation in the measured EWs of the sample giants (25–750 mÅ), we adopted logarithmic reduced widths:

$$RW_{\text{He}} = \log_{10} \left(\frac{EW_{\text{He}}}{\lambda} \right),$$

where EW is in Å. The value $RW_{\text{He}} = -4.85$ was adopted as the threshold for classifying stars with either weak or strong $\lambda 10830$ transitions (C. Sneden et al. 2022). To understand the relation between chromospheric He I strength and photospheric Li abundance among RGB and CHeB stars, we grouped the sample stars based on the amount of Li in them. Since the definition of Li-richness varies with the evolutionary stage of the stars, a stage-specific classification is required (E. N. Kirby et al. 2016). Following the study by R. Singh et al. (2021), we divided RC stars into three groups: Li-normal (RC_{LN} ; $A(\text{Li}) \leq 1.0$), Li-rich (RC_{LR} ; $1 < A(\text{Li}) < 3.2$), and super-Li-rich (SLR; $A(\text{Li}) \geq 3.2$ dex). In the case of RGB stars, we made them into two groups: Li-normal (RGB_{LN} ; $A(\text{Li}) \leq 1.7$ dex) and Li-rich (RGB_{LR} ; $A(\text{Li}) > 1.7$ dex; Y. J. Liu et al. 2014). In

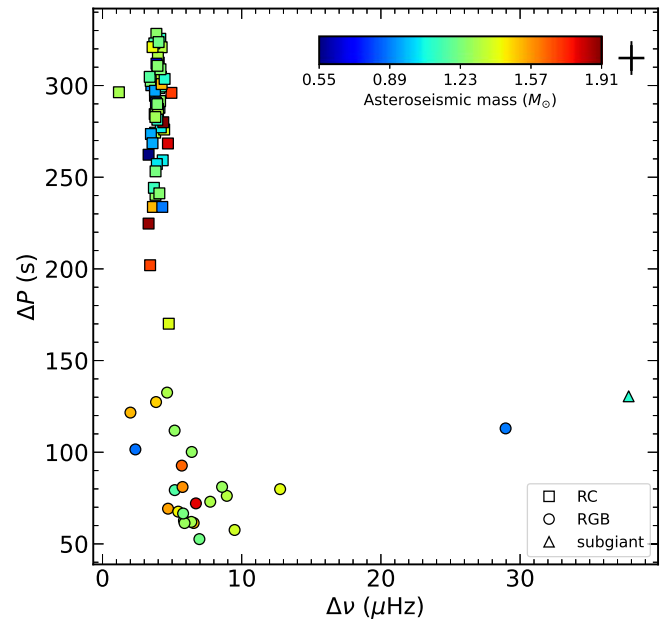


Figure 8. Average ΔP vs. $\Delta \nu$ for all stars. The error cross in the upper right corner indicates typical uncertainties in ΔP and $\Delta \nu$.

Figure 9 we show the entire sample in a plot of $A(\text{Li})$ and RW_{He} for both RC and RGB stars. Of all 58 CHeB stars, 31 exhibit weaker He lines, while 27 display stronger He lines. However, within the 31 SLR group stars, the majority (20) show stronger He I profiles, compared to 11 stars with weaker He I lines. Among 19 RC_{LR} stars, 12 have weaker He lines, while 7 display stronger lines. The subgiant star shows weak He absorption. In the RC_{LN} group, all members exhibit weaker He lines. Among the 24 RGB stars, 3 are situated at the vertical shaded region, while the remaining 21 stars exhibit weak signal.

7. Lithium and He I $\lambda 10830$ Strengths: Influencing Variables

In addition to the He flash, there are alternative proposals for elevated Li among RC giants such as mergers or binary interactions. Several recent works offer insights into the mechanisms driving Li enhancement during binary evolution. A. R. Casey et al. (2019) proposed that tidal spin-up from a binary companion could instigate internal mixing, thereby triggering Li production through the A. G. W. Cameron & W. A. Fowler (1971) mechanism. According to this model, such enhancement might occur randomly at any point along the RGB or the clump phase. Alternatively, X. Zhang et al. (2020) suggest that Li-rich stars in the CHeB phase could be produced through mergers in an RGB + helium white dwarf binary system, where the transfer of angular momentum from a companion leads to the ejection of stellar material, increased stellar rotation, and the formation of dust grains that result in infrared excess. Further observational support comes from R. Singh et al. (2024), who found that a star exhibiting high $A(\text{Li})$ and rotational velocity, along with evidence of a binary companion, likely underwent tidal synchronization following the He flash. Likewise, A. Susmitha et al. (2024) studied metal-poor SLR giants and proposed that past mergers, rather than binarity alone, could explain elevated Li levels, especially

¹³ <http://www.as.utexas.edu/chris/spectre.html>

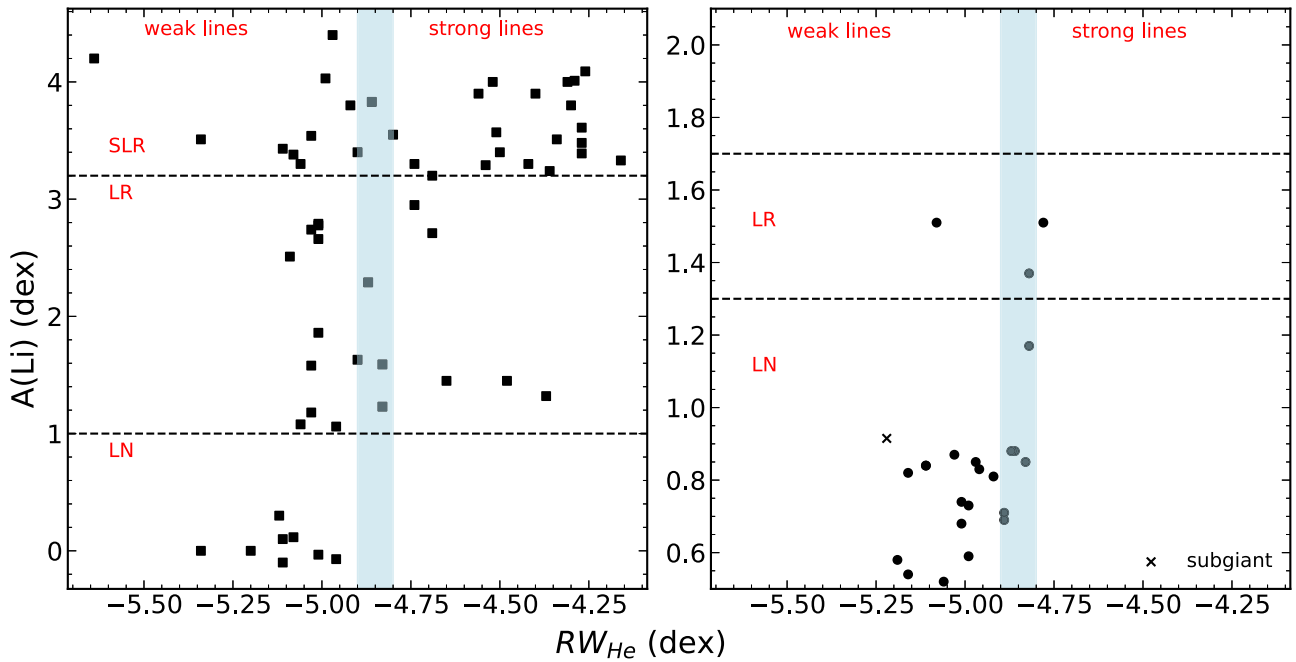


Figure 9. Correlation between RW_{He} and Li abundances. The left panel showcases RC stars, while the right panel showcases RGB stars. Both plots feature a vertical blue shaded region that distinguishes between weak and strong $\lambda 10830$ absorption strengths. Additionally, black dotted lines are used to categorize the stars into Li-normal (LN), Li-rich (LR), and Super Li-rich (SLR) groups. Notably, the right panel identifies a single subgiant among the RGBs, marked with a cross.

during the core helium burning phase, and suggested that these stars might be in the early AGB phase.

We tried to investigate the presence (or absence) of binary companions and infrared excess in our sample by checking for photometric and astrometric variations.

7.1. IR Excess

We gathered optical, near-IR, and mid-IR photometry data from the Virtual Observatory SED Analyzer (VOSA) filter repository, developed by the Spanish Virtual Observatory project. These data were employed to construct optical-IR spectral energy distributions (SEDs) for all sources. We determined the photospheric contribution to the SEDs using F. Castelli & R. L. Kurucz (2003) model atmospheres. Stellar parameters were either derived from existing literature or obtained from LASSP (for stars with calculated Li abundances in this study). VOSA determines the slope of the linear regression of the stellar SED iteratively, adding new infrared data points. It flags an object for IR excess if the slope is significantly smaller (<2.56) than expected from stellar photospheric emission. VOSA further refines IR excess by comparing observational and synthetic flux at each photometric point, identifying significant ($>3\sigma$) deviations as indications of IR excess. A more extensive explanation is available in the VOSA documentation.¹⁴ None of the sample giants show any near-IR/mid-IR excess. However, given the absence of far-infrared data for our objects, we cannot dismiss the possibility of cooler dust around them.

7.2. Binarity

We examined our sample for the presence of astrometric and eclipsing binaries. The Gaia renormalized unit weight error

(RUWE) serves as a valuable indicator for identifying astrometric binaries, with a threshold value exceeding 1.4 suggesting the presence of unresolved binary systems (J.-L. Halbwachs et al. 2023). Only two stars, KIC 10716853 and KIC 10404994, have $RUWE > 1.4$. We also cross-matched our sample with the Hipparcos-Gaia Catalog of Accelerations (HGCA; T. D. Brandt 2021) to leverage their longer baseline for identifying binaries with slightly larger separations. Only four stars from our sample are present in the HGCA. HGCA provides χ^2 values for a constant proper-motion model with 2 degrees of freedom. We converted this χ^2 value to a format similar to Gaia RUWE. Following C. Sneden et al. (2022), HGCA RUWE values >3 suggest the presence of long-term astrometric variations. The same two stars also display HGCA $RUWE > 3$. However, both stars are in the RC phase, with weak He lines and low Li abundances.

To identify potential eclipsing binaries in our sample, we compared our data set with the Kepler Eclipsing Binary Catalog¹⁵ (B. Kirk et al. 2016), which comprises 2920 eclipsing/ellipsoidal binaries extracted from the complete data set of the primary Kepler mission (Q0–Q17). No binary signatures were observed in any of the sample giants. Employing a time-domain RV survey could help in determining spectroscopic binary characteristics in the sample.

7.3. Other Chromospheric Activity Indicators

One of the key indicators of chromospheric activity in cool stars is the presence of nonthermal emission reversals in the central regions of the Ca II H and K absorption lines, located at 3968.470 and 3933.663 Å, respectively. Chromospheric activity in cool stars is commonly expressed using the

¹⁴ <http://svo2.cab.inta-csic.es/theory/vosa/helpw4.php?otype=star&action=help&what=&seeall=1>

¹⁵ [http://\\$Kepler\\$ebs.villanova.edu/](http://$Kepler$ebs.villanova.edu/)

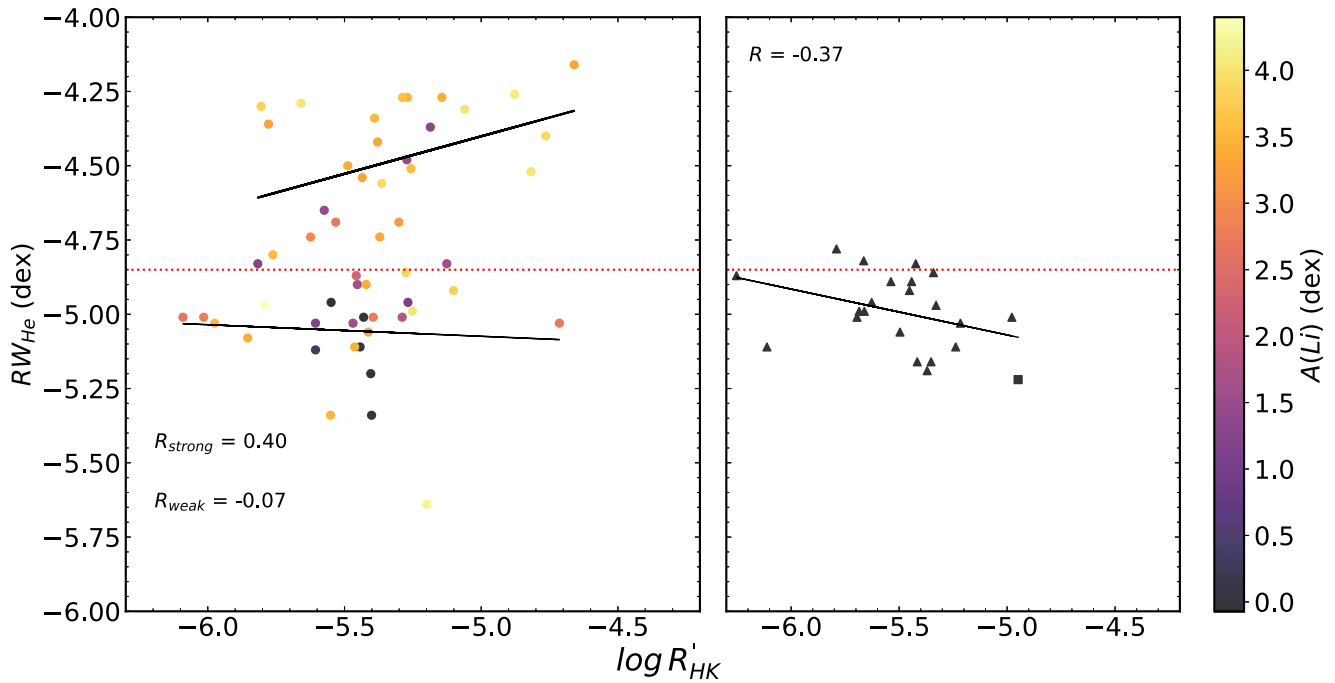


Figure 10. Relationship between RW_{He} and $\log R'_{\text{HK}}$ for RC (left panel) and RGB (right panel) stars. Points are color-coded based on their $A(\text{Li})$ values, with a square marking the position of a single subgiant. The red vertical line differentiates stars with strong and weak He I $\lambda 10830$ absorption lines (C. Sneden et al. 2022). Solid black lines represent correlation trends within the data.

dimensionless S -index:

$$S_{\text{CaII}} = \frac{F_H + F_K}{F_B + F_R},$$

where F_H , F_K , F_B , F_R are the integrated fluxes in the Ca II H and K lines over a triangular bandpass ($\Delta\lambda_{\text{HK}}$) of FWHM 1.09 \AA and the blue and red rectangular pseudocontinuum regions of width ($\Delta\lambda_{\text{BR}}$) 20 \AA centered around 3901.070 and 4001.070 \AA , respectively.

To account for the photospheric contribution to chromospheric emission and the temperature dependence of B and R fluxes, a modified index is devised (R. W. Noyes et al. 1984), which is expressed as

$$R'_{\text{HK}} = R_{\text{HK}} - R_{\text{phot}},$$

where $R_{\text{HK}} = 1.34 \times 10^{-4} C_{\text{cf}} \times S_{\text{MW}}$ and R_{phot} accounts for photospheric correction. The coefficient C_{cf} is dependent on $(B - V)$ color and converts the S -index to R_{HK} , adjusting for temperature-related variations in B - and R -band fluxes. For evolved stars it was defined by R. G. M. Rutten (1984):

$$\log C_{\text{cf}} = -0.066(B - V)^3 - 0.25(B - V)^2 - 0.49(B - V) + 0.45.$$

The photospheric contribution was given by R. W. Noyes et al. (1984):

$$\log R_{\text{phot}} = -4.898 + 1.918(B - V)^2 - 2.893(B - V)^3.$$

S_{CaII} is converted to the Mount Wilson S -index S_{MW} defined by A. H. Vaughan et al. (1978):

$$S_{\text{MW}} = \alpha \times 8 \times \frac{\Delta\lambda_{\text{HK}}}{\Delta\lambda_{\text{BR}}} \times S_{\text{CaII}}.$$

The factor of 8 is due to the design of the original Mount Wilson spectrophotometer, which utilized a quickly rotating slit mask, leading to the H and K channels being exposed for eight times the duration of the reference pseudocontinuum channels, and $\alpha = 1.8$ was adapted from J. C. Hall et al. (2007).

We calculated S_{CaII} for 76 of the 84 stars that satisfied the selection criteria using ACTIN¹⁶ (J. Gomes da Silva et al. 2021), which include spectra with $S/N_g > 10$ in the g band and fewer than 1% negative flux values in the Ca II H and K line bandwidths. To evaluate the accuracy of these measurements, a comparison was made with the data set provided by C. Gehan et al. (2022), which included 37 stars common to both samples. The analysis yielded a mean difference of 0.07 and a standard deviation of 0.003 between the two data sets. S_{CaII} was converted to $\log R'_{\text{HK}}$ using the above relations.

To check for a potential relationship between these two chromospheric activity indicators, we plotted RW_{He} against $\log R'_{\text{HK}}$ for the sample stars in Figure 10, along with the level of $A(\text{Li})$ in stars. For the RC stars (left panel), we observe a moderate positive correlation ($R = 0.40$) within the helium-strong ($RW_{\text{He}} \geq -4.85$) group, suggesting overall enhanced chromospheric activity resulting in increased strengths in both the He I and Ca II lines. In a recent study of the open cluster Stock 2 (M. Jian et al. 2024), a positive correlation was also found between RW_{He} and $\log R'_{\text{HK}}$ for the RC population, in which they observed a much tighter correlation ($R = 0.89$). It might be attributed to the smaller sample size, as only nine giants were studied compared to our 76 giants. However, in the helium-weak RC group, we find a weak negative correlation ($R = -0.11$). This could indicate that they have reached a state of stability following previous shocks. Nevertheless, some level of basal chromospheric activity persists, which is reflected in the observed $\log R'_{\text{HK}}$ values. It is significant to note that

¹⁶ <https://github.com/gomesdasilva/ACTIN2>

relatively more LRGs contribute to the positive correlation. No well-defined correlation among weaker He RC giants probably means that strengths of Ca II and He I evolve differentially following the enhanced activity due to the He flash. In case of RGB stars, we observe a moderately strong negative correlation ($R = -0.4$). Since the He flash has not yet occurred in these stars, their chromospheric dynamics may be more stable and primarily influenced by long-term activity drivers. These stable conditions likely suppress any significant enhancement in Ca II emissions, which could explain the observed negative correlation.

8. Discussion

Recently, a similar study searching for correlations between $A(\text{Li})$ and chromospheric He I $\lambda 10830$ was conducted on a large sample of giants (C. Sneden et al. 2022). This study provided a broader hint that high $A(\text{Li})$ and the strength of the chromospheric He line are correlated; the Li-rich ($A(\text{Li}) > 1.5$ dex) giants are more likely to have stronger He I strength compared to Li-poor ($A(\text{Li}) \leq 1.5$ dex) giants. The key difference between the current and the previous study is that in the current study we have evolutionary phase information for the sample giants. Though the sample in the present study is relatively smaller, it is better constrained in terms of the evolutionary phase. The data for RC and RGB giants are shown in a plot of $A(\text{Li})$ versus RW_{He} in Figure 9. From the figure we make the following observations:

1. None of the RC_{LN} or RGB_{LN} giants (see Section 6) are in the strong He I regime, i.e., $RW_{\text{He}} > 4.80$ dex as defined in C. Sneden et al. (2022).
2. Of the 18 RC_{LR} giants, 9 are He weak, 5 are He strong, and 4 are on the uncertainty band. Among RGB_{LR} giants, none seem to be clearly He strong.
3. The majority (20 out of 29) of SLR RC giants show strong He line strength. Four are on the broader vertical band. The remaining ones are He weak.

The key result is the clear absence of high Li abundance and strong He I profiles on the RGB, while both features are prominent among RC giants. The correlation between them suggests that both strong He I lines and high Li in RC giants may have a common origin, most probably the He flash. However, it is not clear why the RGB giants have a relatively weaker He $\lambda 10830$ line compared to the RCs. Is it due to the He flash in RC stars triggering higher chromospheric activity, leading to stronger He lines, or is it because the interior He-rich material, a by-product of the H-burning shell, is dredged up to the photosphere and then the chromosphere through some flash-induced mixing event?

The He $\lambda 10830$ line strength has been studied extensively in evolved red giants (G. T. J. Obrien & D. L. Lambert 1986; G. H. Smith et al. 2004; A. K. Dupree et al. 2011). However, the impact of the He flash on this line has not been explored. The core helium flash in red giants triggers a complex series of events that can affect the chromosphere. The helium flash generates a thermal pulse, causing a rapid increase in temperature in the core. The increased thermal pressure expands the outer layers of the star rapidly. The outward-moving material from the helium flash can generate shock waves as it interacts with the layers above. These shock waves

can propagate through the stellar atmosphere, disrupting the chromosphere and inducing transient dynamic disturbances. The thermal pulse, expansion, and shock waves may be collectively contributing to enhanced He $\lambda 10830$ absorption. In summary, this study shows that the main He flash and the following subflashes may hold the key for the enhanced He $\lambda 10830$ line among RC giants.

In the case of RGB giants, the absence of He-strong giants may be due to lesser chromospheric activity and also cooler temperatures compared to the stars following He flash. We further discuss below the evolution of chromospheric He and the Li abundance in stars following He flash in light of the results obtained from the asteroseismic analysis.

8.1. Li Abundance—Chromospheric He I Strength Correlation and Their Evolution Following He Flash

Apart from clear separation between giants before and after the He flash in terms of their He I line strengths, we could also notice from Figure 9 a steady decrease in the number of He-strong giants with decreasing Li abundances. It is also true for RGB giants, which have mostly weak absorption profiles. This is very important to note, as the SLR giants are young RCs, i.e., these have very recently undergone He flash and the Li-normal giants are old RCs (see R. Singh et al. 2021). If the He flash is the event that is driving both high Li abundance and chromospheric He I line strength, then both these properties must be evolving with time following He flash. This means that one would expect depleted Li abundance and lesser chromospheric activity among old RC giants. Results in Figure 9 provide evidence that chromospheric He I line strength and the Li abundances are related and evolving with time. The strength of the chromospheric He I line appears to be linked to chromospheric activity rather than an increased He abundance. The subtle correlation between the Ca II H and K indices and RW_{He} among RC_{LR} giants provides further support for this hypothesis, suggesting that the enhanced He I line strengths are likely a result of heightened chromospheric activity induced by the He flash.

To further understand the temporal evolution of Li along with the chromospheric activity, we have shown the relation between ΔP , $A(\text{Li})$, and RW_{He} in Figure 11. ΔP is known to trace the evolution of giants' core from RGB to the RC. As shown in Figure 11, the RGB giants (open circles) are clearly separated in the $A(\text{Li})$ versus ΔP plot with less $A(\text{Li})$ and a weak He I line. Although the $A(\text{Li})$ versus ΔP relation is not well defined, we observe that, on average, younger RC stars (with relatively smaller values of ΔP) tend to have more SLR giants with strong He I lines, compared to older RC giants (with $\Delta P \sim 320$ s), which are mostly Li-normal with weak He I lines. The relation is more noticeable in a plot of $A(\text{Li})$ versus $\Delta \Pi_1$. The asymptotic period spacing ($\Delta \Pi_1$) of the dipole g -mode is understood to be a better representative asteroseismic parameter linked to the core evolution. However, this is only computed for giants that have much better quality data with long cadence. The younger RCs with an average $\Delta \Pi_1 \sim 260$ s are found to be more likely to be SLR with strong He I lines compared to older RCs with an average value of $\Delta \Pi_1 \sim 300$ s (see R. Singh et al. 2021).

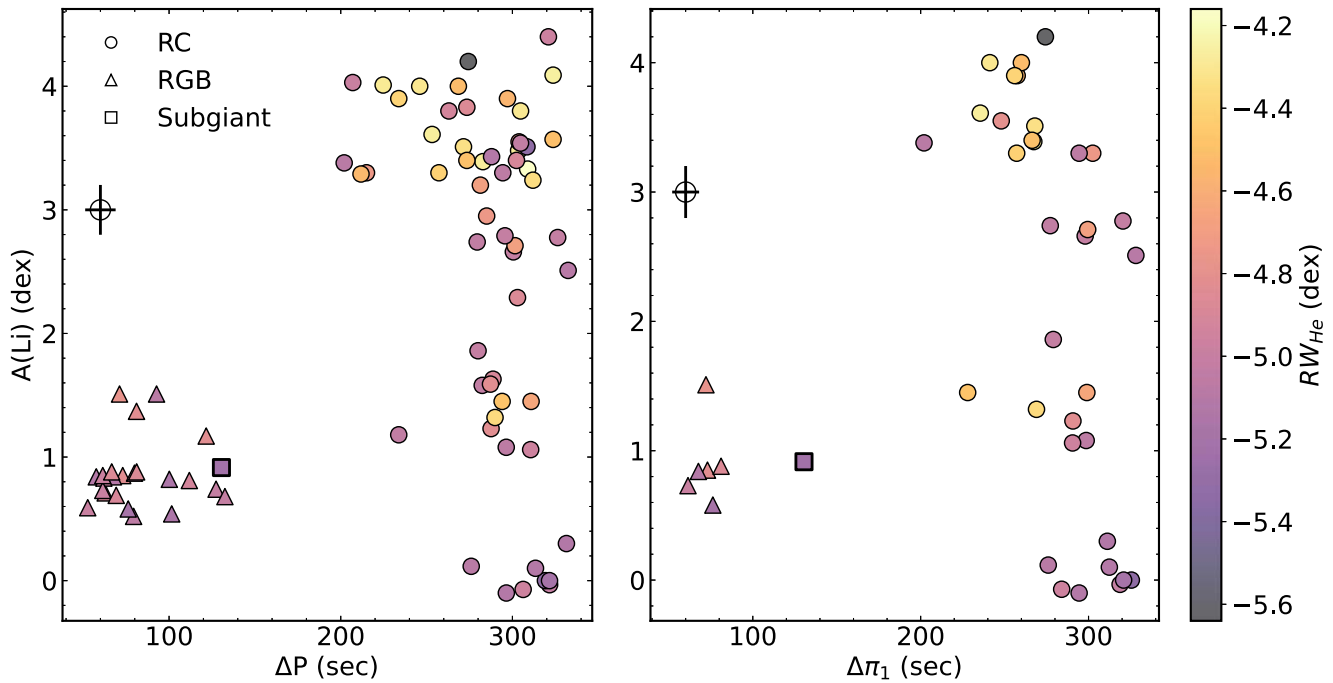


Figure 11. Comparison of $A(\text{Li})$ vs. ΔP (left panel) and $A(\text{Li})$ vs. $\Delta\Pi_1$ (right panel). ΔP is measured for all stars in this study, while $\Delta\Pi_1$, which solely reflects core information, is more sensitive to the time evolution of events following the He flash and is available for 41 stars from the literature. Points in both panels are color-coded according to RW_{He} values.

9. Conclusions

In this study, we analyzed asteroseismic data, chromospheric He I $\lambda 10830$ line strengths, and photospheric Li abundances for 84 giants in the Kepler field to investigate the origin of high Li in RC giants. Our findings reveal a clear distinction between RGB and RC giants in both Li abundance and chromospheric activity. RGB giants exhibit subdued chromospheric activity, weaker He I lines, and lower Li, while RC giants are characterized by strong He I lines and high Li abundance. Notably, we observe a decline in the number of He-strong giants with decreasing Li abundance, consistent with the transient nature of high Li among RC giants.

Our results suggest that He-strong and LRGs are likely younger RC stars, whereas Li-normal and He-weak RC giants are older. The presence of a few SLR giants with weak He I lines indicates that these properties may evolve on different timescales, reflecting variations in the impact of the He flash. Furthermore, we find stronger Ca II H and K emission indices among SLR giants, supporting the hypothesis that this transient enhanced chromospheric activity due to the He flash contributes to both He I and Ca II features.

Looking ahead, it remains unclear whether the strength of the He I line is more influenced by local chromospheric conditions like density and temperature or by transient disturbances caused by the core He flash. Modeling the chromosphere would help clarify this, and in doing so, we can translate our measured EWs into chromospheric He abundances. Additionally, as suggested by B. P. Hema & G. Pandey (2014), their method using MgH bands in optical spectra (for cool stars without photospheric He lines) could help establish relations between photospheric and chromospheric He abundances in connection with the He flash. This would require higher-resolution optical spectra. Asteroseismic data can also be used to study acoustic glitches from the He ionization zone. By calibrating these glitches against models of known He

abundance (K. Verma et al. 2014), we could determine photospheric He abundances, offering an alternative to spectroscopic methods.

Acknowledgments

These results are derived from data collected using the Habitable Zone Planet Finder Spectrograph mounted on the Hobby–Eberly Telescope. The authors extend their gratitude to the Telescope Operators at HET for the precise execution of observations using HPF. The Hobby–Eberly Telescope is a collaborative effort between the University of Texas at Austin, Pennsylvania State University, Ludwig-Maximilians-Universität München, and Georg-August Universität Göttingen. The HET is named in recognition of its principal benefactors, William P. Hobby and Robert E. Eberly. The collaboration acknowledges the assistance and resources provided by the Texas Advanced Computing Center. The authors also wish to acknowledge funding from NSF grants AST-1616040 (C.S.), AST-1908892 (G.N.M.), and TÜBITAK project No. 112T929 (M.A.).

This work makes use of publicly available data from LAMOST DR10 v2.0 (released 2024 September). The Guoshoujing Telescope (LAMOST), a National Major Scientific Project, was built by the Chinese Academy of Sciences. Funding for LAMOST has been provided by the National Development and Reform Commission, and the telescope is operated and managed by the National Astronomical Observatories, Chinese Academy of Sciences.

We gratefully acknowledge the entire Kepler and TESS teams, as well as all those involved in the missions, for their invaluable contributions. Funding for the Kepler mission is provided by NASA’s Science Mission Directorate. All of the data presented here were obtained from the Mikulski Archive for Space Telescopes (MAST).

Facilities: HET (Habitable Zone Planet Finder Spectrograph), LAMOST, MAST.

Software: linemake (V. M. Placco et al. (2021), <https://github.com/vmplacco/linemake>), IRAF (D. Tody 1986, 1993), SPECTRE (M. J. Fitzpatrick & C. Sneden 1987; C. Sneden et al. 2012), Goldilocks (https://github.com/grzeimann/Goldilocks_Documentation), pyMOOGi (<https://github.com/madamow/pymoogi>), Lightkurve (Lightkurve Collaboration et al. 2018), pySYD (A. Chontos et al. 2022), ACTIN 2 (J. Gomes da Silva et al. 2018; J. Gomes da Silva et al. 2021).

ORCID iDs

Anohita Mallick  <https://orcid.org/0000-0002-4282-605X>
 Christopher Sneden  <https://orcid.org/0000-0002-3456-5929>
 Bacham E. Reddy  <https://orcid.org/0000-0001-9246-9743>
 Melike Afşar  <https://orcid.org/0000-0002-2516-1949>

References

- Alcalá, J. M., Biazzo, K., Covino, E., Frasca, A., & Bedin, L. R. 2011, *A&A*, **531**, L12
- Andrae, R., Fouesneau, M., Creevey, O., et al. 2018, *A&A*, **616**, A8
- Asplund, M., Grevesse, N., Sauval, A. J., & Scott, P. 2009, *ARA&A*, **47**, 481
- Bedding, T. R., Mosser, B., Huber, D., et al. 2011, *Natur*, **471**, 608
- Borucki, W. J., Koch, D., Basri, G., et al. 2010, *Sci*, **327**, 977
- Brandt, T. D. 2021, *ApJS*, **254**, 42
- Brown, T. M., Latham, D. W., Everett, M. E., & Esquerdo, G. A. 2011, *AJ*, **142**, 112
- Cameron, A. G. W., & Fowler, W. A. 1971, *ApJ*, **164**, 111
- Casey, A. R., Ho, A. Y. Q., Ness, M., et al. 2019, *ApJ*, **880**, 125
- Castelli, F., & Kurucz, R. L. 2003, in IAU Symp. 210, Modelling of Stellar Atmospheres, ed. N. Piskunov, W. W. Weiss, & D. F. Gray (San Francisco, CA: ASP), **A20**
- Catala, C. & COROT Team 2001, *JAD*, **7**, 8
- Chontos, A., Huber, D., Sayeed, M., & Yamsiri, P. 2022, *JOSS*, **7**, 3331
- Coughlin, J., Thompson, S. E. & Kepler Team 2017, AAS Meeting, **230**, 102.04
- Cybert, R. H., Fields, B. D., & Olive, K. A. 2008, *JCAP*, **2008**, 012
- Deepak, & Reddy, B. E. 2019, *MNRAS*, **484**, 2000
- Dupree, A. K., Strader, J., & Smith, G. H. 2011, *ApJ*, **728**, 155
- Fitzpatrick, M. J., & Sneden, C. 1987, *BAAS*, **19**, 1129
- García Pérez, A. E., Allende Prieto, C., Holtzman, J. A., et al. 2016, *AJ*, **151**, 144
- Gehan, C., Gaulme, P., & Yu, J. 2022, *A&A*, **668**, A116
- Gomes da Silva, J., Figueira, P., Santos, N., & Faria, J. 2018, *JOSS*, **3**, 667
- Gomes da Silva, J., Santos, N. C., Adibekyan, V., et al. 2021, *A&A*, **646**, A77
- Halbwachs, J.-L., Pourbaix, D., Arenou, F., et al. 2023, *A&A*, **674**, A9
- Hall, J. C., Lockwood, G. W., & Skiff, B. A. 2007, *AJ*, **133**, 862
- Handberg, R., & Lund, M. N. 2014, *MNRAS*, **445**, 2698
- Hema, B. P., & Pandey, G. 2014, *ApJL*, **792**, L28
- Holanda, N., Drake, N. A., & Pereira, C. B. 2020, *AJ*, **159**, 9
- Holtzman, J. A., Hesselquist, S., Shetrone, M., et al. 2018, *AJ*, **156**, 125
- Hon, M., Stello, D., Garcia, R. A., et al. 2019, *MNRAS*, **485**, 5616
- Huber, D., Stello, D., Bedding, T. R., et al. 2009, *CoAst*, **160**, 74
- Iben, I. J. 1968, *ApJ*, **154**, 581
- Jian, M., Fu, X., Matsunaga, N., et al. 2024, *A&A*, **687**, A189
- Katz, D., Sartoretti, P., Guerrier, A., et al. 2023, *A&A*, **674**, A5
- Kirby, E. N., Guhathakurta, P., Zhang, A. J., et al. 2016, *ApJ*, **819**, 135
- Kirk, B., Conroy, K., Prša, A., et al. 2016, *AJ*, **151**, 68
- Kumar, Y. B., Reddy, B. E., Campbell, S. W., et al. 2020, *NatAs*, **4**, 1059
- Kumar, Y. B., Reddy, B. E., & Lambert, D. L. 2011, *ApJL*, **730**, L12
- Lightkurve Collaboration, Cardoso, J. V. d. M., Hedges, C., et al., 2018
 Lightkurve: Kepler and TESS time series analysis in Python, Astrophysics Source Code Library, ascl:1812.013
- Liu, Y. J., Tan, K. F., Wang, L., et al. 2014, *ApJ*, **785**, 94
- Lomb, N. R. 1976, *Ap&SS*, **39**, 447
- Magrini, L., Smiljanic, R., Franciosini, E., et al. 2021, *A&A*, **655**, A23
- Mahadevan, S., Ramsey, L., Bender, C., et al. 2012, *Proc. SPIE*, **8446**, 84461S
- Mahadevan, S., Ramsey, L. W., Terrien, R., et al. 2014, *Proc. SPIE*, **9147**, 91471G
- Mallick, A., Singh, R., & Reddy, B. E. 2023, *ApJL*, **944**, L5
- Martell, S. L., Simpson, J. D., Balasubramaniam, A. G., et al. 2021, *MNRAS*, **505**, 5340
- Mitler, H. E. 1972, *Ap&SS*, **17**, 186
- Mosser, B., Benomar, O., Belkacem, K., et al. 2014, *A&A*, **572**, L5
- Noyes, R. W., Hartmann, L. W., Baliunas, S. L., Duncan, D. K., & Vaughan, A. H. 1984, *ApJ*, **279**, 763
- O'Brien, G. T. J., & Lambert, D. L. 1986, *ApJS*, **62**, 899
- Pinsonneault, M. H., Charbonnel, C., & Deliyannis, C. P. 2000, in IAU Symp. 198, The Light Elements and their Evolution, ed. L. da Silva, R. de Medeiros, & M. Spite (Cambridge: Cambridge Univ. Press), **74**
- Placco, V. M., Sneden, C., Roederer, I. U., et al. 2021, *RNAAS*, **5**, 92
- Preston, G. W., Sneden, C., & Chadid, M. 2022, *AJ*, **163**, 109
- Romano, D., Matteucci, F., Ventura, P., & D'Antona, F. 2001, *A&A*, **374**, 646
- Ruchti, G. R., Fulbright, J. P., Wyse, R. F. G., et al. 2011, *ApJ*, **743**, 107
- Rutten, R. G. M. 1984, *A&A*, **130**, 353
- Sackmann, I. J., & Boothroyd, A. I. 1992, *ApJL*, **392**, L71
- Scargle, J. D. 1982, *ApJ*, **263**, 835
- Sharma, S., Stello, D., Bland-Hawthorn, J., Huber, D., & Bedding, T. R. 2016, *ApJ*, **822**, 15
- Singh, R., Mallick, A., Reddy, B. E., Pandey, J. C., & Zhao, G. 2024, *ApJL*, **971**, L3
- Singh, R., Reddy, B. E., Bharat Kumar, Y., & Antia, H. M. 2019, *ApJL*, **878**, L21
- Singh, R., Reddy, B. E., Campbell, S. W., Kumar, Y. B., & Vvard, M. 2021, *ApJL*, **913**, L4
- Smith, G. H., Dupree, A. K., & Strader, J. 2004, *PASP*, **116**, 819
- Smith, J. C., Stumpe, M. C., Van Cleve, J. E., et al. 2012, *PASP*, **124**, 1000
- Smith, V. V., Plez, B., Lambert, D. L., & Lubowich, D. A. 1995, *ApJ*, **441**, 735
- Sneden, C., Afşar, M., Bozkurt, Z., et al. 2021, *AJ*, **161**, 128
- Sneden, C., Afşar, M., Bozkurt, Z., et al. 2022, *ApJ*, **940**, 12
- Sneden, C., Uomoto, A., Cottrell, P., & Fitzpatrick, M., 2012 SPECTRE: Manipulation of single-order spectra, Astrophysics Source Code Library, ascl:1202.010
- Sneden, C. A. 1973, PhD thesis, Univ. Texas, Austin
- Stello, D., Chaplin, W. J., Basu, S., Elsworth, Y., & Bedding, T. R. 2009, *MNRAS*, **400**, L80
- Susmitha, A., Mallick, A., & Reddy, B. E. 2024, *ApJ*, **966**, 109
- Takeda, Y., & Tajitsu, A. 2017, *PASJ*, **69**, 74
- Ting, Y.-S., Hawkins, K., & Rix, H.-W. 2018, *ApJL*, **858**, L7
- Tody, D. 1986, *Proc. SPIE*, **627**, 733
- Tody, D. 1993, in ASP Conf. Ser. 52, Astronomical Data Analysis Software and Systems II, ed. R. J. Hanisch, R. J. V. Brissenden, & J. Barnes (San Francisco, CA: ASP), **173**
- Tsantaki, M., Delgado-Mena, E., Bossini, D., et al. 2023, *A&A*, **674**, A157
- Van Cleve, J. E., & Caldwell, D. A. 2009, Kepler Instrument Handbook, Kepler Science Document KSCI - 19033 (Moffett Field, CA: NASA-Ames Research Center)
- Vaughan, A. H., Preston, G. W., & Wilson, O. C. 1978, *PASP*, **90**, 267
- Verma, K., Faria, J. P., Antia, H. M., et al. 2014, *ApJ*, **790**, 138
- Vvard, M., Mosser, B., & Samadi, R. 2016, *A&A*, **588**, A87
- Walker, G., Matthews, J., Kuschnig, R., et al. 2003, *PASP*, **115**, 1023
- Wallerstein, G., & Sneden, C. 1982, *ApJ*, **255**, 577
- Wang, S.-G., Su, D.-Q., Chu, Y.-Q., Cui, X., & Wang, Y.-N. 1996, *ApOpt*, **35**, S155
- Xiang, M. S., Liu, X. W., Yuan, H. B., et al. 2015, *MNRAS*, **448**, 822
- Yan, H.-L., Zhou, Y.-T., Zhang, X., et al. 2021, *NatAs*, **5**, 86
- Zhang, X., Jeffery, C. S., Li, Y., & Bi, S. 2020, *ApJ*, **889**, 33